

# **Forecasting and Measuring Radio Interference due to Mega Constellations**

by

Artem Davydov

A THESIS SUBMITTED IN PARTIAL FULFILLMENT OF  
THE REQUIREMENTS FOR THE DEGREE OF

BACHELOR OF SCIENCE

in

The Faculty of Science

(Physics and Astronomy)

THE UNIVERSITY OF BRITISH COLUMBIA

(Vancouver)

May 2022

© Artem Davydov 2022

# Abstract

The Low Earth Orbit population of communication satellites is set to increase rapidly in the next few decades. Thousands of satellites are already in orbit with tens of thousands more approved by the FCC. The characteristic down link frequency used by the satellite operators is either the \*Ku (12–18 GHz) or the \*X (8–12GHz) band (\*IEEE). The potential impact of these satellites on astronomical measurements carried out in the radio regime are unknown. Although some collaborations like the Square Kilometer Array Organization have undertaken the task of modelling the potential impact. The SKA organization found that a population of approximately 100,000 satellites will render the Ku band unusable for radio observations in that regime. The Canadian Galactic Emission Mapper Telescope is a planned radio telescope that will target the 8–10GHz radio sky. The frequency range was chosen to fill in the gap in polarized sky observations already carried out and the betterment of Galactic foreground modelling which relies on ideally a complete coverage of frequency space. To forecast the impact of satellites on the CGEM survey we modelled satellite state vectors using the SGP4 orbit propagator feeding it SpaceX satellites Two Line Elements (TLEs) provided by NORAD. We used the telescope’s parameters, satellite flux densities, and telescope-satellite geometry to compute when a satellite intersects the telescope’s bore-sight. We produce plots of satellite counts within an angle  $\theta = 0.1, 0.5, 1.0$  of CGEM’s bore-sight. We present plots of the duty cycles and plots of the expected power intercepted by CGEM from the satellites in Watts. We constructed a digital acquisition system hosted on the ZCU111 evaluation board. The digital back-end was coupled to a TV analog front end. We measured the response of our system to radiation incoming to the ground to be 5 dB brighter than that incoming from the sky. Inspection of histogram of the two measurements shows no evidence of strong radio interference detectable by the current configuration of the system.

# Table of Contents

<b>Abstract</b> . . . . .	ii
<b>Table of Contents</b> . . . . .	iii
<b>List of Figures</b> . . . . .	iv
<b>Acknowledgements</b> . . . . .	xii
<b>1 Introduction</b> . . . . .	1
1.1 Motivation . . . . .	1
1.2 The Canadian Galactic Emission Mapper (CGEM) Telescope	6
<b>2 Theory</b> . . . . .	8
2.1 Satellite State Vectors . . . . .	8
2.1.1 Coordinate Frames . . . . .	10
2.1.2 Time Conventions Note . . . . .	10
2.1.3 Principle Rotations . . . . .	11
2.2 Measuring Radio Waves . . . . .	13
<b>3 Experimental Methods</b> . . . . .	16
3.1 Event Modelling . . . . .	16
3.2 Link Budget Analysis . . . . .	17
3.3 Radio Interference Monitor . . . . .	23
3.3.1 Analog Domain . . . . .	23
3.3.2 Digital Domain . . . . .	23
<b>4 Results</b> . . . . .	27
<b>5 Discussion</b> . . . . .	34
<b>6 Conclusion</b> . . . . .	36
<b>Bibliography</b> . . . . .	37

# List of Figures

- 1.1 A cartoon of the atmospheric window of electromagnetic radiation. The top horizontal ruler provides a scale of the wavelengths of electromagnetic radiation in nano-meters, increasing to the left. Note that the two largest gaps with no significant absorption coincide with the visible (650-1200nm) and radio wavelengths(approximately 1cm-10m). These are indicated by gaps in the bottom bar of the figure. The majority of the spectrum is opaque to our atmosphere. (Credit: NASA Radio JOVE Project) . . . . . 1

## *List of Figures*

- 1.2 Plotted in blue is the count of total space launches and the orange plot corresponds to payloads (e.g. satellites). The launch and payload counts are binned per year spanning from 1957 to the 2022-02-04. Data were obtained using Space-Tracks data access API. The payload to launch ratio remained close to 1 from the year 1957 to approximately the year 2010. We observe a sharp increase in payloads from the year 2010 continuing through February of 2022. The sharp decrease in launch and payload counts in 2022 is a result of data being available only for January and February of 2022. The sharp increase in the ratio of payload to launch is a result of innovative reusable rocketry which lowers the cost of launch to orbit. Another factor is the capability of operators such as SpaceX to inject dozens of satellites into low earth orbit per launch. The total count of launches per year remains steady below 250. This is due to the shifting of relative contribution of each country. Annual launch data categorized by nation obtained from Space-Track indicates that Russia's annual launch rate has been decreasing steadily since the late 1990's while China has started growing its launch rate around that period. The United States' annual launch rate decreased around the late 1960's but remained steady since with approximately 30 launches per year. . . . .

1.3 A photo from a 333 second exposure taken by DECam on the Blanco 4-meter telescope at the Cerro Tololo Inter-American Observatory (CTIO). The streaks correspond to satellites of the StarLink constellation. Pixels with light contamination from these satellites lose viability deeming them unusable for inference of astrophysical information. (Credit: NOIRlab) . . .

---

*List of Figures*

---

- 2.1 Depicted is an annotated two line elements (TLE) data set for the Q3B FM5 satellite. The first line contains the name of the satellite. The subsequent two lines both start with the satellite number. The second line contains the international designator, epoch of the satellite, first and second values of the positional derivatives at the epoch and the drag coefficient. The third line lists the orbital elements: orbital inclination, right ascension of ascending node, argument of perigee, mean anomaly, mean motion, and number of current revolution of the satellite. The two line element data set encapsulates the minimum amount of information necessary for reliable orbit reconstruction. [Credit: SatSig.net] . . . . . 8
- 2.2 A cartoon of a Keplerian orbit with key two line element orbital parameters labelled. The orbital inclination,  $i$ , is measured from the projection of the periapsis line to the projection of the periapsis line onto the equatorial plane. The periapsis is the point at which the satellite is closest to the central object which in our context is the earth. The argument of periapsis is the angular extent measured from the ascending node  $N_1$  (a vector pointing to the point where the object passes from below the reference plane (equatorial plane) to the volume above the reference plane) to the periapsis vector. The longitude of ascending node,  $\Omega$ , is measured from the Vernal Equinox to the ascending node. The longitude can be calculated from the the right ascension of the ascending node provided in the TLE's. The descending node  $N_2$  is a vector pointing to the point where the oject in orbit crosses from above to below the reference plane (equatorial). These parameters are sufficient to orient the orbital plane with respect of the equatorial plane for any satellite. The dynamical parameters (mean motion, 1st derivative, and 2nd derivative) are also provided with the TLE's are necessary to solve for the position of the satellite in the elliptical orbit as a function of time. The SGP4 algorithm takes as input these parameters and outputs the ephemeris data for the corresponding satellite. . . . . 9

## *List of Figures*

*List of Figures*

---

- 3.1 A polar plot of the co-pol (right hand circular) in green and x-pol (left hand circular) in blue of a potential beam had feed design of CGEM produced using TICRA by Josh MacEachern of the UBC experimental cosmology lab. The angular extend of the plot was limited to  $50 \leq \theta \leq 50$  where the 0 angle coincides with the bore sight direction. The radial direction measures the response of the beam in units of dBi. The main lobe extends between  $-0.5 \leq \theta \leq 0.5$  (filled with pink) with a beam response of 50dBi across the extend of the main lobe. The secondary region extending between  $-10 \leq \theta \leq 10$  marks the boundaries where the beam response exceeds 0 dBi. The rest of the beam response never exceeds the 0 dBi threshold in any direction. Note that the intercepted power is penalized by 50 dBi for power incoming from beyond  $\theta \approx 10$  of the beam. This model inform our beam response for calculating the power intercepted by CGEM from satellites. . . . . 19
- 3.2 Depicted are traces (blue dots) of 100 StarLink Satellite orbits propagated using the SGP4 algorithm for the time window between: 2021-12-29T12:30:31 to 2021-12-30T12:30:30. The Dominion Radio Astrophysics Observatory is marked with a black dot on a wire mesh sphere (red) representing a sphere with approximately the radius of the earth ( 6,400km). Note that the orbital plane drifts in time resulting in lines thicker than the diameter of a single point. Most of orbital planes plotted correspond to an inclination of approximately  $i = 50$ , which is consistent with the distribution of orbital inclination detailed in SpaceX's FCC filings. . . . . 22
- 3.3 Plotted are three duty cycles for all StarLink satellite assets downloaded from the SatTrak website on December 27th, 2021. The y axis measures the number of satellites within a cone centered at CGEM's boresight direction vector. Three different cone angular extents were plotted  $\epsilon = 0.5, 5,$  and  $10$  (top to bottom). The SGP4 model extrapolated the state vectors to the time window between: 2021-12-29T12:30:31 to 2021-12-30T12:30:30. As the cone extent is increased more satellites become visible however the power intercepted is penalized according to the beam response of the model hat feed. The beam response to both RHC and LHC radiation incoming from sources beyond  $\theta = 10$  is below 0 dBi. . . . . 24

## *List of Figures*

- 3.4 A block diagram depicting the high level design of the RFI monitor. The left most component in the diagram corresponds to the television dish the will be used for the system. The dish is an off-axis, 33 inch diameter, parabolic reflector with a housing for an LNB. We used the SatMaximum Universal Single LNB (SM 2010-01) with an integral feed horn and a standard 40mm neck. These LNBs are designed for satellite television receiver dishes and are normally connected to a TV box which mixes down the signal to an intermediate frequency and then decoded. To utilize the LNB in the absence of a TV box we introduce a bias tee between the LNB and the ADC acquisition system. The LNB accepts two settings inputs: a DC current level of 13V or 18V to switch between horizontal and linear polarization setting respectively. The local oscillator frequency is controlled by an input tone of 0KHz or 22KHz corresponding to a local oscillator frequency of 9.75GHz or 10.6GHz respectively. The output of the bias tee is fed to the ADC on the Xilinx ZCU111 evaluation board. The ADC set to sample the signal at 4GSPS in 8 microsecond bursts. . . . .

26

4.1 The blue curve in the plot corresponds to time series data taken using our digital acquisition system with the feed horn pointed up. We have taken 10 samples each capturing of length  $8\mu\text{s}$ . The blue curve is comprised of 10 of these samples plotted sequentially. The data was binned to 1000 bins prior to plotting. The red horizontal line denotes the average voltage of the up oriented measurement and lies at  $\mu = -0.00011\text{V}$ . The solid horizontal green line corresponds to the voltage two positive deviation from the mean where  $\sigma = 0.00015\text{V}$ . The dashed black line corresponds to the voltage value two negative standard deviations away from the mean. The majority of voltage measurement appear to lie within  $2\sigma$  of the mean value. We do not observe dramatic changes in the voltage that may correspond to strong radio contaminants.

*List of Figures*

---

- 4.2 The blue curve in the plot corresponds to time series data taken using our digital acquisition system with the feed horn pointed down. The red horizontal line denotes the average voltage of the up oriented measurement and lies at  $\mu = -0.00012V$ . The solid horizontal green line corresponds to the voltage two positive deviation from the mean where  $\sigma = 0.00015V$ . The dashed black line corresponds to the voltage value two negative standard deviations away from the mean. The majority of voltage measurement appear to lie within  $2\sigma$  of the mean value. We do not observe dramatic changes in the voltage that may correspond to strong radio contaminants just as in the case of up pointing measurement. . . . . 29
- 4.3 Shown in green is a histogram of the voltage time series data binned to 200 bins. The vertical axis measures the counts of occurrences withing each voltage bin. The horizontal axis measured the voltage and corresponds to the histogram bins. The curve in blue is a Gaussian fit to the histogram data with  $\sigma = 0.00309$ . The histogram of the up pointing time series data appears to be excellently described by a Gaussian function. We do not observe a high energy tail that could correspond to a radio frequency contaminant in the 10.7-12.7GHz band. . . . . 30
- 4.4 Shown in blue is a histogram of the voltage time series data binned to 200 bins. The vertical axis measures the counts of occurrences withing each voltage bin. The horizontal axis measured the voltage and corresponds to the histogram bins. The curve in orange is a Gaussian fit to the histogram data with  $\sigma = 0.00562$ . The histogram of the up pointing time series data appears to be excellently described by a Gaussian function. We do not observe a high energy tail that could correspond to a radio frequency contaminant in the 10.7-12.7GHz band just as the histogram of the up pointing measurement time series data. . . . . 31

## *List of Figures*

- 4.5 The blue curve corresponds to the real part of the Fourier transform of the time series data obtained by pointing the horn feed down. The red curve is the real part of the Fourier transform of the time series data obtained by pointing the horn feed up. The plot truncated the Fourier transform at half the sampling frequency of our ADC system (4GHz). The real Fourier components are provided in units of dB as a function of frequency. We see a rise in power between 0-1GHz. This behavior may be accounted for by the side bands of the LNB. We see that in the range between 1-2GHz the power intercepted from the down pointing measurement exceeds the power intercepted from the up pointing measurement by approximately 4-6 dB for all frequencies in that range. This observation strengthens our confidence in the ability of the digital acquisition system to unambiguously distinguish between sources of brightness temperature of order 300K (the earth) and approximately 25K (the sky). . . . .

4.6 The blue curve corresponds to the difference taken between the binned real parts of the FFT of the down and up pointing time series data. The vertical axis measures the power response of our acquisition system in decibels. The horizontal axis measures the frequency in hertz. We observe that the difference between the up and down measurement rises between 0-1GHz until it plateaus at approximately 5 dB for frequencies between 1-2GHz. We interpret this result as an unambiguous difference between the brightness ground and the sky on the order of 5 dB in the frequency range between 10.7-12.7 GHz corresponding to the input frequency of the LNB. . . . .

# Acknowledgements

I would like to thank my supervisors Dr. Mark Halpern and Dr. Gary Hinshaw for the opportunity to explore. I would also like to thank Parham Zarei (MSc) of the UBC Experimental Cosmology for his relentless work on the digital acquisition system.

# Chapter 1

## Introduction

### 1.1 Motivation

The microwave frequency range represents a limited portion of the electromagnetic spectrum that is not absorbed by the atmosphere. This makes the microwave frequency a natural choice for telecommunication operators and many earth based astronomical observations. An explanatory diagram is shown in figure 1.1.

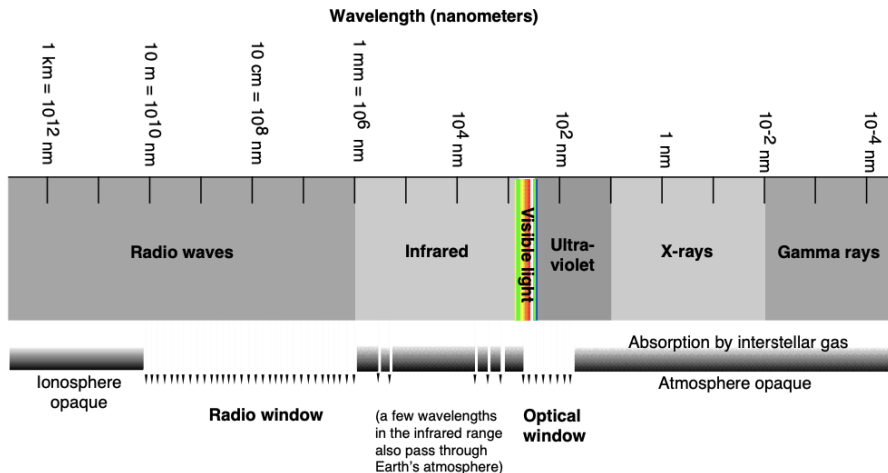


Figure 1.1: A cartoon of the atmospheric window of electromagnetic radiation. The top horizontal ruler provides a scale of the wavelengths of electromagnetic radiation in nano-meters, increasing to the left. Note that the two largest gaps with no significant absorption coincide with the visible (650-1200nm) and radio wavelengths(approximately 1cm-10m). These are indicated by gaps in the bottom bar of the figure. The majority of the spectrum is opaque to our atmosphere. (Credit: NASA Radio JOVE Project)

Electromagnetism is a wave like phenomena. The principle of superposition dictates that if we were to measure the electromagnetic field at

### *1.1. Motivation*

---

any point in space, we would be measuring the contribution from all source of radiation passing through the point in that time. The measured signal is simply the sum of all electromagnetic radiation passing through that point. Radio astronomical apparatus is designed to measure radio signals received from the sky which are characteristically orders of magnitude less relative to artificial sources of radiation such as cellphone towers or television satellites. A radio receiver integrated into a telescope is susceptible to interference from telecommunication satellites due to the sharing of a common band. In the last decade multiple companies received authorization by the FCC to launch satellite constellation to provide global internet[3][4][5]. These constellations range in size between dozens to hundreds per orbital planes and elevation angle. Space-Track.org is a website that provides an open access API to launch data. According to payload and launch data binned by year obtained on 2022-02-04 from Space-Track, the payload per launch ratio increased by a factor of almost 1000 between the years 2010 and 2022[14]. The trend appears to maintain a positive slope up to the time of writing this thesis. A plot of the payload, launch, and year data is shown in figure 1.2.

### 1.1. Motivation

---

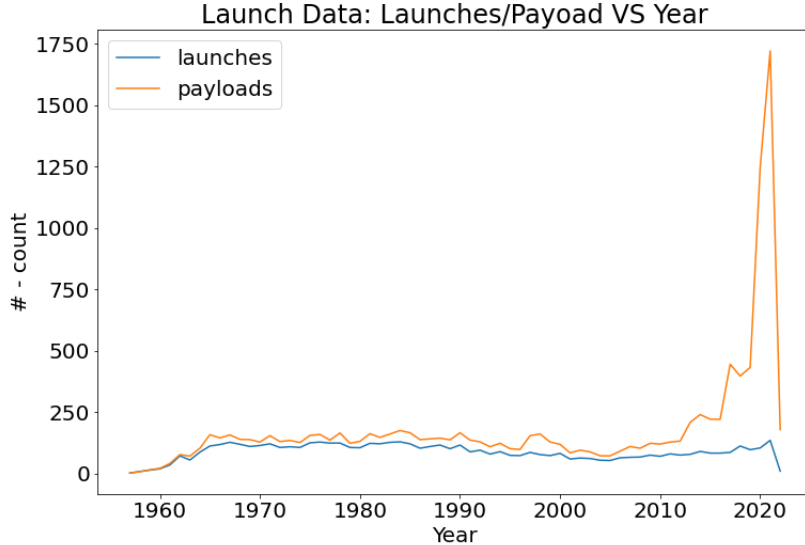


Figure 1.2: Plotted in blue is the count of total space launches and the orange plot corresponds to payloads (e.g. satellites). The launch and payload counts are binned per year spanning from 1957 to the 2022-02-04. Data were obtained using Space-Tracks data access API. The payload to launch ratio remained close to 1 from the year 1957 to approximately the year 2010. We observe a sharp increase in payloads from the year 2010 continuing through February of 2022. The sharp decrease in launch and payload counts in 2022 is a result of data being available only for January and February of 2022. The sharp increase in the ratio of payload to launch is a result of innovative reusable rocketry which lowers the cost of launch to orbit. Another factor is the capability of operators such as SpaceX to inject dozens of satellites into low earth orbit per launch. The total count of launches per year remains steady below 250. This is due to the shifting of relative contribution of each country. Annual launch data categorized by nation obtained from Space-Track indicates that Russia's annual launch rate has been decreasing steadily since the late 1990's while China has started growing its launch rate around that period. The United States' annual launch rate decreased around the late 1960's but remained steady since with approximately 30 launches per year.

Note that these data are not limited to commercial launches and include instrument payloads and space missions. Each of these satellites commu-

### *1.1. Motivation*

---

nicates with the customer and its ground station in the X-Ku band (10.7-12.7GHz). Radiation from an ensemble of these satellites can potentially swamp significant astrophysical signals. Such effects can be mitigated by the telescope designers but this requires an understanding of the expected radio background on site. Some of the satellites used by operators are capable of modulating the radiation flux they transmit to the surface of the earth [6]. The impact of SatCom constellations on astronomy was felt by optical astronomers in November 2019. The Cerro Tololo Inter-American Observatory (CTIO) released photos from a 333 seconds-exposure where at least 19 bright streaks are visible. The streaks are attributed to reflections off of a "train" of StarLink satellites[2] with brightness comparable to some of the brightest astrophysical objects in the field of view. The photograph is shown in figure 1.3.

### 1.1. Motivation

---

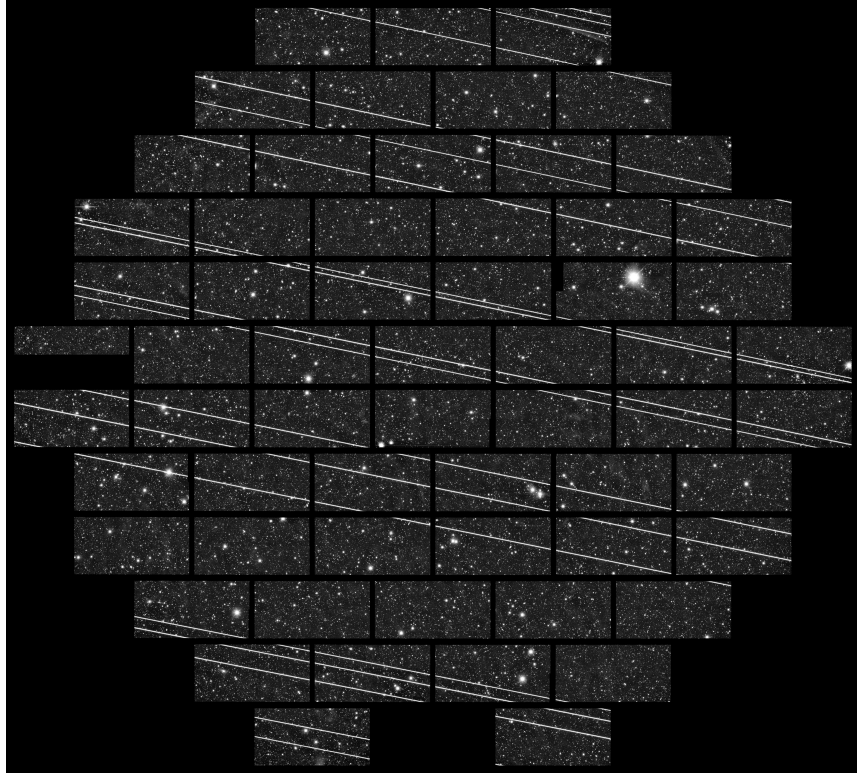


Figure 1.3: A photo from a 333 second exposure taken by DECam on the Blanco 4-meter telescope at the Cerro Tololo Inter-American Observatory (CTIO). The streaks correspond to satellites of the StarLink constellation. Pixels with light contamination from these satellites lose viability deeming them unusable for inference of astrophysical information. (Credit: NOIRlab)

The StarLink constellation's down-link frequency coincides with the receiver frequency on the Square Kilometer Array (SKA) Mid telescope located in South Africa. An analysis performed by the SKA organization predicts that for a constellation of significantly large size (100,000 satellites) potentially threatens the viability of their entire observation band[1]. Co-operation between operators and astronomers will be of utmost importance in the scenario where large portions of the microwave band is saturated by telecommunication signals. In addition to the observed and potential astrophysical impact of super-constellations there is a true risk of accelerating the "Kessler Syndrome". Donald J. Kessler is a Orbital Debris and Meteoroid Consultant who devoted much of his career to interplanetary meteoroid en-

## 1.2. The Canadian Galactic Emission Mapper (CGEM) Telescope

---

vironment and early orbital debris modelling. In 1978 Kessler published *Collision Frequency of Artificial Satellites: The Creation of a Debris Belt* where he predicted that the density of catalogued items (objects whose trajectories are known) will increase to a point where inter-object collision will become the primary debris production mechanism. Kessler later clarified the term "Kessler's Syndrome" which was popularized by the media and adopted by the orbital debris community:

"The *Kessler Syndrome* was meant to describe the phenomenon that random collisions between objects large enough to catalogue would produce a hazard to spacecraft from small debris that is greater than the natural meteoroid environment. In addition, because the random collision frequency is non-linear with debris accumulation rates, the phenomenon will eventually become the most important long-term source of debris, unless the accumulation rate of larger, non-operational objects (e.g., non-operational payloads and upper stage rocket bodies) in Earth orbit were significantly reduced. Based on past accumulation rates, the 1978 publication predicted that random collision would become an important debris source around the year 2000, with the rate of random collisions increasing rapidly after that, if the accumulation rate were not reduced to near zero." [13]

-Donald J. Kessler

The catalogue growth rate in the 1978 paper was 520 object per year. The catalog growth rate based on available data as of February 2022 exceeds 2000 objects per year. If we heed Kessler's warning and implement measures to reduce the accumulation rate of object we can reduce random collision rate thereby reducing the risk of catastrophic collisions. More violent and rapid debris creation mechanisms such as Anti-satellite weapons (ASAT) have become significant over the past few decades [15] and are perhaps more easily avoidable than random collisions between commercial satellites. Based on current growth rates and previous modelling it is evident that a multi-nation initiative is required to avoid catastrophic in orbit events.

## 1.2 The Canadian Galactic Emission Mapper (CGEM) Telescope

The Experimental Cosmology Group at University of British Columbia is currently working on a new radio telescope. The Canadian Galactic Emis-

## *1.2. The Canadian Galactic Emission Mapper (CGEM) Telescope*

---

sion Mapper (CGEM) telescope will observe the 8-10GHz polarized sky. The frequency was chosen to target the Galactic synchrotron emission. The frequency band of CGEM is adjacent to the down link band of the SpaceX Starlink constellation (10.7-12.7 GHz). We developed a computer simulation that models the position of each deployed satellite for a given observation time windows (ephemeris data). These models were used to produce forecasts for the presence of satellite within the telescope line of sight. Using the position and expected radio emission level from satellites we estimated the power intercepted by our dish during the observation window. We also developed a 4GHz digital acquisition system with a X-Ku band analog front end. The analog front end was built using cheaply available over the counter TV dish and a low noise block with feed (LNB). The Radio Frequency Interference (RFI) monitor was deployed at the DRAO site to measure the power intercepted from the sky at 3 different pointings. The severity of radio contamination can be derived from the spectrum of the measurement. RFI expectations derived from ephemeris modelling were correlated with DRAO site measurements taken using our RFI monitor in the time domain. The code used to simulate the ephemeris data and expected power levels will be made widely available to the community. The development of the digital back end was documented and the characterization of the Analog-to-Digital (ADC) converter will be made available to other experimenters and the community as well. Lastly, this project will contribute to the community's understanding of the changing radio sky.

# Chapter 2

## Theory

### 2.1 Satellite State Vectors

Ephemeris data describes the velocity and position vector (the state vectors) of an object in orbit as a function of time. The state vectors of the satellites are reconstructed using up-to-date orbital parameters provided by the North American Aerospace Defence Command (NORAD) in Two Line Element (TLE) format. An example TLE with key parameters annotated in shown in figure 2.1.

Name of satellite	Int. Designation (13=year, A=first item off the launcher )	Epoch	Mean motion	Ephemeris type	
Satellite number		1st deriv	2nd deriv	Drag coeff	Element no
Q3B FM5					
1 39188	U 13031A	14318.21238429	- .00000028	00000-0	00000+0 0 1302
2 39188	0.0402	340.8502	0003409	258.5822	120.5402 5.00116345 25340
Orbit inclination	Right ascension of ascending node	Argument of perigee	Mean anomaly	Mean motion	Revolution no

Figure 2.1: Depicted is an annotated two line elements (TLE) data set for the Q3B FM5 satellite. The first line contains the name of the satellite. The subsequent two lines both start with the satellite number. The second line contains the international designator, epoch of the satellite, first and second values of the positional derivatives at the epoch and the drag coefficient. The third line lists the orbital elements: orbital inclination, right ascension of ascending node, argument of perigee, mean anomaly, mean motion, and number of current revolution of the satellite. The two line element data set encapsulates the minimum amount of information necessary for reliable orbit reconstruction. [Credit: SatSig.net]

Two Line Elements contains 7 orbital parameters used to reconstruct the ephemeris of each satellite. A cartoon of an example earth satellite orbit with the the key geometric orbital parameters labelled is depicted in figure 2.2.

## 2.1. Satellite State Vectors

---

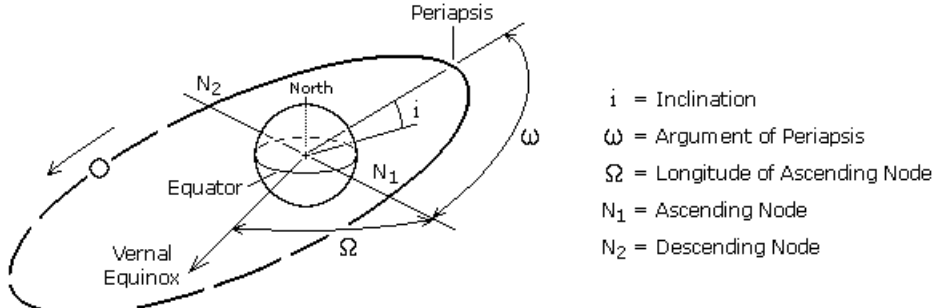


Figure 2.2: A cartoon of a Keplerian orbit with key two line element orbital parameters labelled. The orbital inclination,  $i$ , is measured from the projection of the periapsis line to the projection of the periapsis line onto the equatorial plane. The periapsis is the point at which the satellite is closest to the central object which in our context is the earth. The argument of periapsis is the angular extent measured from the ascending node  $N_1$  (a vector pointing to the point where the object passes from below the reference plane (equatorial plane) to the volume above the reference plane) to the periapsis vector. The longitude of ascending node,  $\Omega$ , is measured from the Vernal Equinox to the ascending node. The longitude can be calculated from the right ascension of the ascending node provided in the TLE's. The descending node  $N_2$  is a vector pointing to the point where the object in orbit crosses from above to below the reference plane (equatorial). These parameters are sufficient to orient the orbital plane with respect of the equatorial plane for any satellite. The dynamical parameters (mean motion, 1st derivative, and 2nd derivative) are also provided with the TLE's are necessary to solve for the position of the satellite in the elliptical orbit as a function of time. The SGP4 algorithm takes as input these parameters and outputs the ephemeris data for the corresponding satellite.

Solving for the orbit of the satellites amounts to solving Kepler's Equation which does not have a closed form solution[16]. The Spacetrak Report NO.3 by Hoots and Roehrich describes a numerical algorithm, the Simplified General Perturbations model (SGP4), which solves the equation given the orbital parameters. The algorithm also accounts for effects such as gravitational perturbations and orbital decay due to drag[17]. SGP4 is available as a Python package which we used, along side NORAD's TLE's for StarLink's satellites, to produce state vectors for the constellation for a full 24 hours

## 2.1. Satellite State Vectors

---

period with 10 seconds resolution.

### 2.1.1 Coordinate Frames

The following frames of reference provide the context in which all further vector quantities are manipulated: the DRAO frame, the TEME frame, and the telescope frame. The definitions for the telescope and DRAO frames were laid out by Josh MacEachern from the UBC experimental Cosmology group in an internal document [18]. The majority of subsequent calculations will be carried out in the DRAO frame. The frame moves with the rotation of the earth and is rigidly attached to the surface of the earth at  $\lambda = 49^\circ 19' 15'' \text{N}$ , and  $\phi = 119^\circ 37' 15'' \text{W}$ . The DRAO coordinate vectors are:

$$\begin{cases} \hat{\mathbf{X}}_{\text{DRAO}}, & \text{DRAO Zenith} \\ \hat{\mathbf{Y}}_{\text{DRAO}}, & \text{North} \\ \hat{\mathbf{Z}}_{\text{DRAO}}, & \text{East} \end{cases}$$

The telescope frame is attached to the DRAO frame on a gimbal allowing it to be arbitrarily oriented as the physical telescope would. The articulation of the telescope frame will be achieved using rotation matrices parametrized using Euler angles. The initial configuration of the telescope frame with respect to the DRAO frame is summarized next:

$$\begin{cases} \hat{\mathbf{X}}_{\text{TEL}}, & \text{South} \\ \hat{\mathbf{Y}}_{\text{TEL}}, & \text{East} \\ \hat{\mathbf{Z}}_{\text{TEL}}, & \text{DRAO Zenith} \end{cases}$$

The True Equator Mean Equinox (TEME) frame is an earth centred inertial frame (non accelerating/ rotating) and is defined with respect to the mean equatorial plane and the earth sphere:

$$\begin{cases} \hat{\mathbf{X}}_{\text{TEME}}, & \text{Vernal Equinox} \\ \hat{\mathbf{Y}}_{\text{TEME}}, & \text{s.t RH System} \\ \hat{\mathbf{Z}}_{\text{TEME}}, & \text{North Pole} \end{cases}$$

### 2.1.2 Time Conventions Note

The orbital parameters are approximately valid with respect to an epoch. The epoch encodes a year, days, and decimal UTC of day and is provided as part of the TLE data set [17]. All dates and times used in our calculations

## 2.1. Satellite State Vectors

---

were expressed in terms of Julian date and a fractional part of a Julian date. The Julian date was converted to Unix time (seconds) for the purpose to calculating the telescope rotation matrices. This is due to the convenience of expressing the azimuthal phase at time  $t$  as a product of the angular velocity in radians per second and the current Unix time.

### 2.1.3 Principle Rotations

An arbitrary rotation of a frame  $F_2$  with respect to a fixed frame  $F_1$  can be achieved by a composition of rotation matrices parameterized using the Euler angles  $\theta, \phi$  and  $\psi$ . This formalism is necessary to describe the position of the bore sight vector as a function of time with respect to the local DRAO frame. We introduced the *TEL* subscript to denote the Euler angles of the telescope with respect to a fixed DRAO frame. The coordinate transformation geometry is shown in figure 2.3.

## 2.1. Satellite State Vectors

---

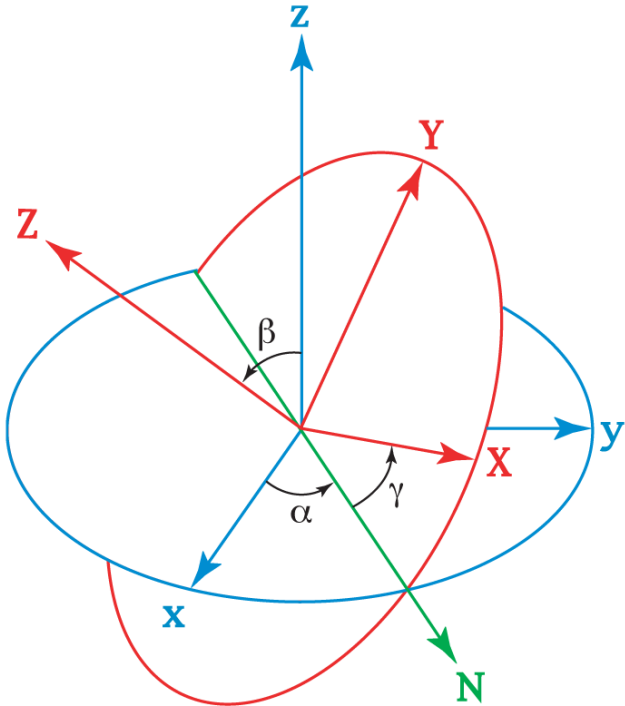


Figure 2.3: Plotted are two perpendicular coordinate systems: F1(red) a fixed coordinate system comprised of the three axis: x, y, and z. F2 (blue) is attached with a gimbal to the F1 system's (0,0,0) origin point and is denoted by the capitalized letters: X, Y, and Z. The Euler angles:  $\alpha$ ,  $\beta$ , and  $\gamma$  keep of the angular magnitude of rotations. Any rotation of F2 with respect to F1 can be specified using the Euler angles and the sequence of axis with the respect to which the rotation is carried out from left to right in order. The rotation described in the figure can be described by the list z-X'-Z" and the Euler angles. This rotation can be described as follows: rotate the F2 frame counter clock wise (CCW) by an angle  $\alpha$  about the z axis, then rotate the F2 system about the X' axis (where the prime axis denote the original frame after a single rotation) by an angle  $\beta$ , finally rotate the F2 frame about the axis Z" by and angle  $\gamma$ . Where gamma is measured from the line of nodes N (green) that lies in the intersection between the xy and XY planes to the X axis.

## 2.2 Measuring Radio Waves

The idealized dipole antenna can be used to illustrate the design decisions and theory we considered when choosing the components of our radio interference monitor. An oscillating electric field produces a current across the dipole antenna depicted in figure 2.4.

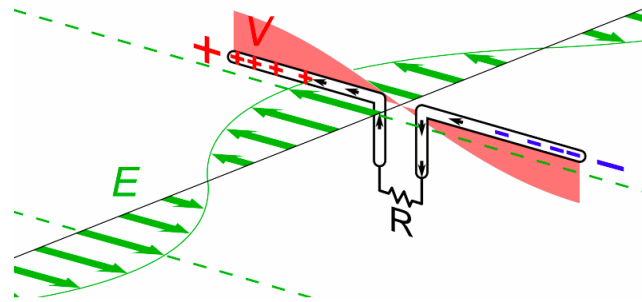


Figure 2.4: A snap shot of an electric field,  $E$ , depicted as green arrows enveloped by oscillating line passing through a dipole antenna. The changing electric field carried by the electromagnetic wave induces a current (black arrows along the antenna) by moving the free charges in the antenna. A resistor,  $R$ , connects the two conducting wires comprising the antenna. A measurable voltage  $V$  (filled red curve perpendicular to  $E$  field plane) is dropped across the resistor. (Credit: Chetvorno, CC0, via Wikimedia Commons)

The energy emitted by a source satellite is expressed in terms of flux density ( $F$ ) and are measured in Watts per meters squared ( $W/m^2$ ). Note that we idealize the satellites as point sources in the sky. The energy intercepted by our dish is therefore:

$$P(t) = \vec{A}(t) \cdot \vec{F}(t) \quad (2.1)$$

Where  $\vec{A}$  points in the direction normal to the surface containing the dish rim in the direction of the sky. The length of the vector is the effective area of the dish  $A = \pi(D/2)^2$  for a dish width diameter  $D$ . The vector  $\vec{F}$  points the direction of the pointing vector and its magnitude is the flux density arriving from the source. Lastly, the resultant dot product  $P(t)$  encodes the electromagnetic energy intercepted by the dish.

Let us denote the voltage dropped across the resistor  $R$  with  $V(t)$ :

## 2.2. Measuring Radio Waves

---

$$V(t) = V_{sky}(t) + V_{interference}(t) + V_{noise}(t) \quad (2.2)$$

The voltage measured includes the contribution of all source including the wanted sky signal and the unwanted system noise and external interference. The sky signal is expected to be faint therefore a low noise amplifier with gain  $G_{RF}$  is required for successful detection. We are interested in a limited bandwidth that will be then digitized. This requires the introduction of a band-pass filter. The band-pass filter can be mathematically represented in the frequency domain using Heaviside functions:

$$F_{bp} = U(\nu - \nu_{up}) - U(\nu_{lo}) \quad (2.3)$$

The output voltage after the band pass is:

$$V_{bp} = F^{-1}(F(V_{RF}(t)G_{RF})F_{bp}) \quad (2.4)$$

Low noise amplifiers with sufficient gain for high frequency signals are expensive. The band limited, high frequency signal is "copied" down to a lower frequency using a mixer. A mixer is a circuit component that multiplies an input signal coming in at a frequency (RF) with a sine wave with an intermediate frequency (IF) and outputs a signal that contains the sums and differences of the frequencies. In the case of a pure harmonic ( $\nu_{RF}$ ) input signal the mixer acts as follows [7]:

$$V_{bp}(t)\sin(2\pi\nu_{IF}t) = \cos[2\pi(\nu_{IF} - \nu_{RF})t] - \cos[2\pi(\nu_{RF} + \nu_{IF})t]$$

Where  $V_{bp}(t) = 2\sin(2\pi\nu_{RF}t)$ , and the mixed down component is given by:

$$V_{IF}(t) = \cos[2\pi(\nu_{IF} - \nu_{RF})t] \quad (2.5)$$

The higher frequency ( $\nu_{RF} + \nu_{IF}$ ) component can be filtered with a low pass filter represented in the frequency domain gain using a Heaviside function:

$$F_{lp} = 1 - U(\nu_{cut}) \quad (2.6)$$

Where  $\nu_{cut}$  is chosen such that the higher frequency component is filtered without losing any of the lower frequency copy at ( $\nu_{RF} - \nu_{IF}$ ). The low frequency signal can now be amplified using cheaper hardware with gain  $G_{IF}$ . Finally, the output voltage of the system is given by:

$$V_{bp}(t) = F^{-1}(F(V_{IF}(t)G_{IF})F_{lp}) \quad (2.7)$$

The output of the cascaded electrical circuit consisting of the antenna, low noise high frequency amplifier, band pass filter, mixer, low pass filer, and finally the intermediate frequency amplifier is fed to an Analog-to-Digital converter. A flow chart is shown in figure 2.5. The theory behind successful digitization of a discretely sampled analog signal is covered next.

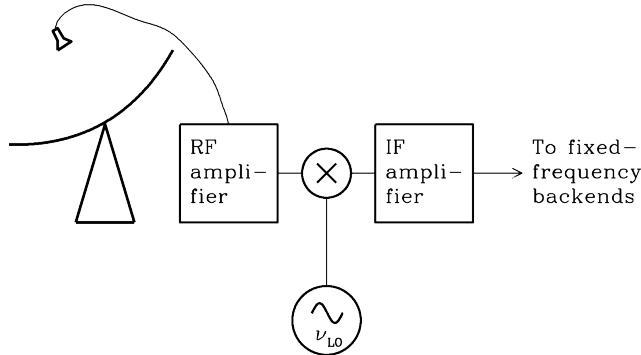


Figure 2.5: A flow chart cartoon of a radio telescope. The radio dish on the left most of the diagram feeds the receiver dangling above it. The receiver is connected to an RF amplifier. The amplifier output to a mixer with a local oscillator operating at a frequency of  $\nu_{lo}$ . The mixer outputs to an intermediate frequency amplifier that is connected to a fixed frequency back-end (right most of the diagram). (Credit: NRAO)

The Nyquist-Shannon condition sets a lower limit on the sampling frequency for which the analog signal can be reliably reconstructed. The Nyquist-Shannon inequality for a band limited input signal is:

$$T < \frac{1}{2\nu_c} \quad (2.8)$$

# Chapter 3

# Experimental Methods

## 3.1 Event Modelling

The orbital parameter elements for a satellite, s, are fed to SGP4 to produce the state vectors at time t.

$$\vec{r}_s(t)_{\text{TEME}}, \vec{v}_s(t)_{\text{TEME}} = \text{SGP4}(TLE_s) \quad (3.1)$$

The state vectors are given in the True Equator Mean Equinox (TEME) frame. We transform the TEME position state vectors to altitude and azimuth pairs,  $(\alpha_s(t), \beta_s(t))$ , of the satellite which are given with respect to the observatory location (DRAO). This conversion was done using Astropy's TEME to altitude and azimuth library. The altitude and azimuth angles are related to the local DRAO frame unit vector pointing at the satellite by:

$$\vec{r}_s(t)_{\text{DRAO}} = \begin{bmatrix} \sin(\alpha_s(t))\cos(\beta_s(t)) \\ \cos(\alpha_s(t))\cos(\beta_s(t)) \\ \sin(\beta_s(t)) \end{bmatrix}_{\text{DRAO}} \quad (3.2)$$

The telescope bore sight vector is orientated at an angle  $\theta_{tel}$  away from zenith at the DRAO. The telescope will rotate at a nominal azimuthal angular velocity  $\omega_{az}$ . We produce unit vectors corresponding to the telescope pointing direction in the DRAO frame at times t by applying a rotation matrix corresponding to: first rotating the telescope frame about  $\hat{x}_{\text{DRAO}}$  clockwise by 40 degrees corresponding to setting  $\theta_{tel} = 40$ . The telescope frame is then rotated counter clockwise about  $\hat{z}_{\text{DRAO}}$  by the time dependent angle  $\phi_{tel} = \omega_{az}(t) - \Delta$  [18]. Where  $\omega_{az} = 4\text{RPMS}$  and  $\Delta$  is a phase term corresponding to an arbitrary initial azimuth phase. The angle phi is measured in the DRAO frame and is subtended by  $\hat{x}$  and  $\vec{B}(t)_{proj}$ , the projection of the boresight vector onto the DRAO X-Y plane. The angle  $\theta_{tel}$  is the co-altitude of the bore-sight vector. This produces the bore-sight vector stack:

$$\vec{B}(t)_{\text{DRAO}} = \mathbf{A}_{\text{TL}} \hat{\mathbf{z}}_{\text{TEL}} \quad (3.3)$$

### 3.2. Link Budget Analysis

---

$$\vec{B}_s(t)_{DRAO} = \begin{pmatrix} \cos \phi'_{tel} & -\sin \phi'_{tel} \cos \theta_{tel} & \sin \phi'_{tel} \sin \theta_{tel} \\ \sin \phi'_{tel} & \cos \phi'_{tel} \cos \theta_{tel} & -\cos \phi'_{tel} \sin \theta_{tel} \\ 0 & \sin \theta_{tel} & \cos \theta_{tel} \end{pmatrix} \begin{bmatrix} 0 \\ 0 \\ 1 \end{bmatrix} \quad (3.4)$$

The angle between the bore-sight vector is defined to be:

$$\aleph_s(t) = \angle(\vec{B}_s(t)_{DRAO}, \vec{r}_s(t)_{DRAO}) \quad (3.5)$$

The satellite position vector at time t was extracted from their dot product:

$$\aleph_s(t) = \cos^{-1} \left( \frac{\text{dot}(\vec{B}(t)_{DRAO}, \vec{r}_s(t)_{DRAO})}{|\vec{B}_s(t)_{DRAO}| |\vec{r}_s(t)_{DRAO}|} \right) \quad (3.6)$$

We define the condition for a in line of sight event as a satellite being within a  $\epsilon_{cone}$  degree cone of the bore sight. We define the hit function H:

$$H_s(t) = \begin{cases} H_s(t) = 1, & |\aleph_s(t)| \leq \epsilon_{cone} \\ H_s(t) = 0, & \text{else} \end{cases}$$

The duty cycle, D, is the number of satellites within the cone of extent  $\epsilon_{cone}$  per time bin where  $s_{tot}$  is the count of satellites in the TLE set:

$$D(t) = \sum_{s=0}^{s_{tot}} H_s(t) \quad (3.7)$$

The International Telecommunications Union (ITU) is a body responsible for allocation of bandwidth and development of standards for communication networks. The ITU put forth a Equivalent Power-Flux Density (EPFD) limit for the protection of Geostationary groups stations from radio interference. The EPFD "takes into account the aggregate of the emission for all non-GSO satellites in the direction of any GSO station" [19]. Space Exploration Technologies Corp's (SpaceX) FCC filings report regarding power flux density (PDF) at earth informs our reference values for the expected flux received by CGEM's receiver. SpaceX calculated EPFD values for their constellations considering their antennas to be iso-emitters.

## 3.2 Link Budget Analysis

The information about the down-link signal was informed by SpaceX's power flux density at the surface of the earth estimates. We combine these data

### 3.2. Link Budget Analysis

---

with simulated beam patterns calculated using an example beam hat design provided by TICRA. TICRA is a reflector, antenna, and EM design suite used by the UBC experimental cosmology group. This paper adopts the link budget terminology common place in telecommunication applications. Link budget analysis is a book-keeping device that keeps track of the gains, losses, transmitted, and received power. The power received by the CGEM telescope is:

$$P_{RX}(dBm) = P_{TX}(dBm) + Gains(dBi) - Losses(dB) \quad (3.8)$$

Note that SpaceX's satellites down-link Right Hand Circular (RHC) radiation therefore our analysis will idealize the satellites as pure RHC radiation emitters [21]. A polar diagram of a potential CGEM beam response to co and cross pol radiation is shown in figure 3.1.

### 3.2. Link Budget Analysis

---

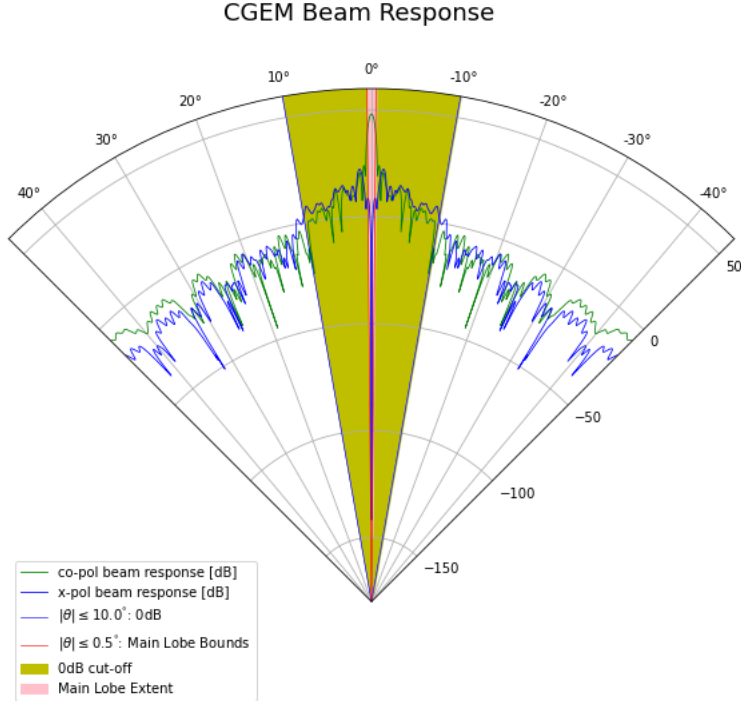


Figure 3.1: A polar plot of the co-pol (right hand circular) in green and x-pol (left hand circular) in blue of a potential beam had feed design of CGEM produced using TICRA by Josh MacEachern of the UBC experimental cosmology lab. The angular extend of the plot was limited to  $50 \leq \theta \leq 50$  where the  $0$  angle coincides with the bore sight direction. The radial direction measures the response of the beam in units of dBi. The main lobe extends between  $-0.5 \leq \theta \leq 0.5$  (filled with pink) with a beam response of 50dBi across the extend of the main lobe. The secondary region extending between  $-10 \leq \theta \leq 10$  marks the boundaries where the beam response exceeds 0 dBi. The rest of the beam response never exceeds the 0 dBi threshold in any direction. Note that the intercepted power is penalized by 50 dBi for power incoming from beyond  $\theta \approx 10$  of the beam. This model inform our beam response for calculating the power intercepted by CGEM from satellites.

### 3.2. Link Budget Analysis

---

The gains and losses of StarLink satellites as well as key CGEM beam response parameters are summarized in table 3.1.

Parameter	Value (Units)
$EIRPin4kHzStarLink$	-10.73 dBW, Slant
$EIRPin1MHzStarLink$	-14.06 dBW, Nadir
$SpreadingLoss_{StarLink}$	-130.24 dB, Slant
$SpreadingLoss_{StarLink}$	-126.91 dB, Nadir
$P_{TXStarLink}$ @ Ku	116.99 dB ( $\frac{W}{m^{-2}}$ ), Nadir
$P_{TXStarLink}$ @ Ku	117.00 dB ( $\frac{W}{m^{-2}}$ ), Slant
$P_{RXCGEM}$ @ 10GHz	50.00 dBi, $\theta = 0^\circ$
$P_{RXCGEM}$ @ 10GHz	0.00 dBi, $\theta \geq 10^\circ$

Table 3.1: We tabulated available gain and loss information for StarLink satellites and the CGEM telescope. StarLink's Effective Isotropic Radiated Power (EIRP), spreading loss, and net transmitted power density at the surface of the earth were fetched from SpaceX's Information Regarding Power Flux Density, Revision 2 filing [9]. StarLink's parameter values are given with respect to two possible geometrical arrangements between a ground station (CGEM) and satellite. Nadir is the point on the earth directly below the satellite (anti-parallel to zenith). Slant corresponds to the angle off nadir restricted by the maximum earth angle seen by the satellite. A potential CGEM reflector with hat feed were modelled using TICRA. The beam response was calculated at 10GHz. The gains provided are for the co-pol response corresponding to right hand circular (RHC) radiation. CGEM gain values are provided with respect to the angle  $\theta$  measured from the nominal bore sight direction of the telescope.

Using the angle between the telescope bore-sight and telescope position, the expected power flux density at earth due to the satellite down link, and CGEM's beam response pattern, we can model the expected power intercepted by the dish as a function of time. We will model the satellites as uniform omni-directional emitter with flux values informed SpaceX's PFD filing.

The power intercepted by the telescope from satellite that is within  $\epsilon_{cone}$  at time  $t$  is approximately:

$$P_s(t) = A_{dish} \cos(\aleph_s(t)) 10^{\frac{F_{Ku} + R(\hat{n})}{10}} [\text{Watts}] \quad (3.9)$$

Where  $R(\hat{n})$  is the response of the parabolic reflector to radiation incoming from the direction  $\hat{n}$  in dB. The unit vector is considered in the telescope

### 3.2. Link Budget Analysis

---

frame. Finally the total power received by the dish at time  $t$  is the sum over all satellites in the constellation:

$$P(t) = \sum_{s=0}^{s_{tot}} P_s(t) \quad (3.10)$$

We produced state vectors for the StarLink constellation TLE (accessed: December 27th, 2021) using the SGP4 library. The time frame under scrutiny is 2021-12-29T12:30:31 to 2021-12-30T12:30:30. The time resolution was set to 10 seconds between each simulated state vector. The state vectors are given in the TEME frame. Orbit traces for 100 StarLink satellites are shown in figure 3.2.

### 3.2. Link Budget Analysis

---

Orbit Traces of 100 StarLink Satellites [(2021-12-29)T12:30:31-T13:00:31]

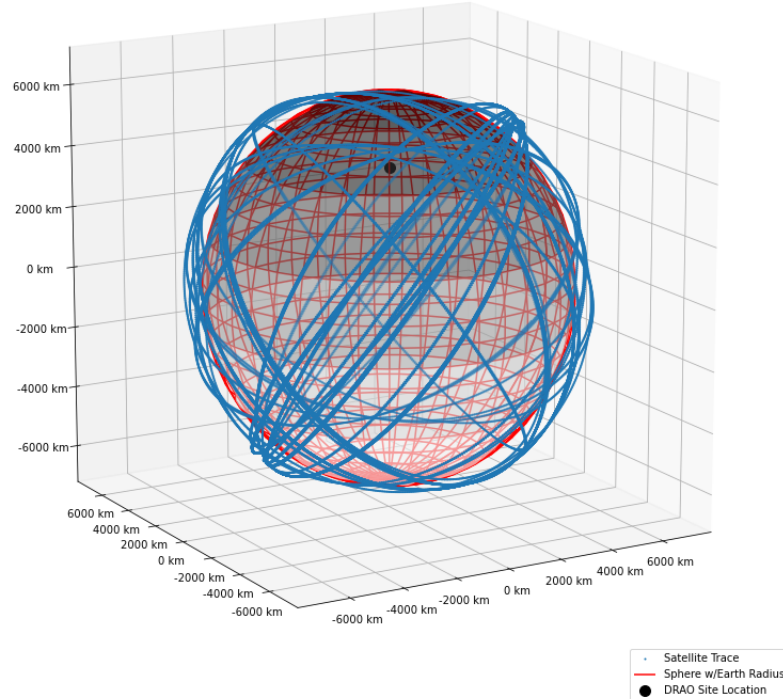


Figure 3.2: Depicted are traces (blue dots) of 100 StarLink Satellite orbits propagated using the SGP4 algorithm for the time window between: 2021-12-29T12:30:31 to 2021-12-30T12:30:30. The Dominion Radio Astrophysics Observatory is marked with a black dot on a wire mesh sphere (red) representing a sphere with approximately the radius of the earth ( 6,400km). Note that the orbital plane drifts in time resulting in lines thicker than the diameter of a single point. Most of orbital planes plotted correspond to an inclination of approximately  $i = 50$ , which is consistent with the distribution of orbital inclination detailed in SpaceX's FCC filings.

### 3.3. Radio Interference Monitor

---

We used the astropy *transformto* library to transform the TME position vector to altitude-azimuth pairs given with respect to the local DRAO frame. We simulated the CGEM bore-sight vector with respect to the DRAO frame for each time step. The separation angle between the bore-sight vectors and satellite position vectors was calculated at each time step and two duty cycles for two separation cut-offs;  $\epsilon = 0.5^\circ$  and  $\epsilon = 5.0^\circ$  are shown in figure 3.3.

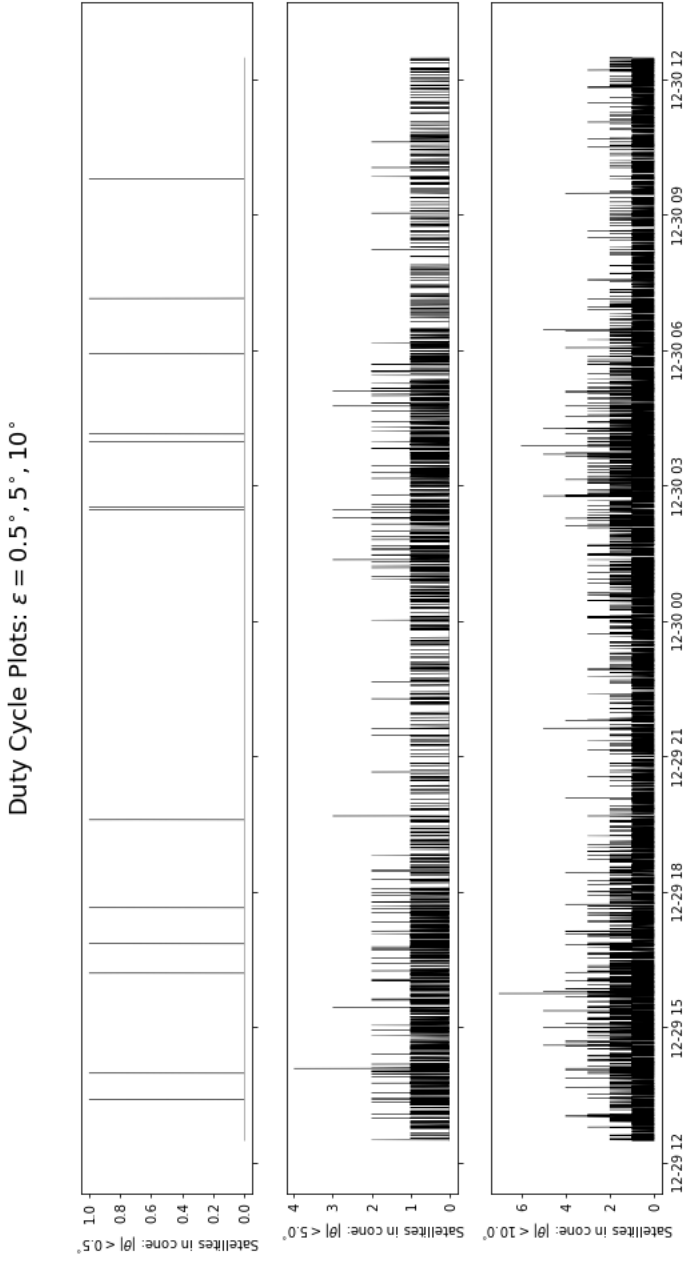
## 3.3 Radio Interference Monitor

### 3.3.1 Analog Domain

We constructed a Ku antenna receiver system to measure the radio interference at the DRAO site. The analog front end was built using a satellite TV dish and a Low Noise Block. The dish used is an off-axis, 33 inch diameter, parabolic reflector with a housing for a Low Noise Block. A Low Noise Block contains a feed horn and an antenna. We used the SatMaximum Universal Single LNB (SM 2010-01) with an integral feed horn and a standard 40mm neck. These LNBs are designed for satellite television receiver dishes and are normally connected to a TV box which mixes down the signal to an intermediate frequency and then decoded. To utilize the LNB in the absence of a TV box we introduced a bias tee between the LNB and the ADC acquisition system. The LNB accepts two settings inputs: a DC current level of 13V or 18V to switch between horizontal and linear polarization setting respectively. The local oscillator frequency is controlled by an input tone of 0KHz or 22KHz corresponding to a local oscillator frequency of 9.75GHz or 10.6GHz respectively. We fed the LNB with a 13V DC signal with no tone corresponding to the LNB being set to measure horizontal polarization and the local oscillator value set to 9.75GHz. The output of the bias tee was fed to our 4GSPS digital back end.

### 3.3.2 Digital Domain

We derived a lower sampling frequency requirement for our digital acquisition systems ADC from the Nyquist-Shannon condition. The expected bandwidth of the CGEM experiment is 2GHz centered at 9GHz. The bandwidth that will be sampled using our RFI monitor is 1GHz. This sets a sliding scale requirement for an ADC sampling frequency of 2-4GHz. A system capable of managing sampling, processing and saving the data at this rate is realizable using available FPGA technology. The digital back




---

Figure 3.3: Plotted are three duty cycles for all StarLink satellite assets downloaded from the SatTrak website on December 27th, 2021. The y axis measures the number of satellites within a cone centered at CGEM's boresight direction vector. Three different cone angular extents were plotted  $\epsilon = 0.5^\circ, 5^\circ$ , and  $10^\circ$  (top to bottom). The SGP4 model extrapolated the state vectors to the time window between: 2021-12-29T12:30:31 to 2021-12-30T12:30:30. As the cone extent is increased more satellites become visible however the power intercepted is penalized according to the beam response of the model hat feed. The beam response to both RHC and LHC radiation incoming from sources beyond  $\theta = 10^\circ$  is below 0 dB<sub>i</sub>.

### *3.3. Radio Interference Monitor*

---

end is hosted on Xilinx's ZCU111 evaluation board. The board is equipped with 8 x 12-bit ADCs with maximum operating rate of 4.096 GSPS[20]. Data are down linked to an SD card in  $8\mu s$  bursts with 12-bit resolution at the full 4GHz bandwidth. The data bursts were time stamped and later combined and analyzed on a local machine. Data processing and analysis is covered in the data analysis section. A block diagram of the RFI monitor analog domain design is shown in figure 3.4.

### 3.3. Radio Interference Monitor

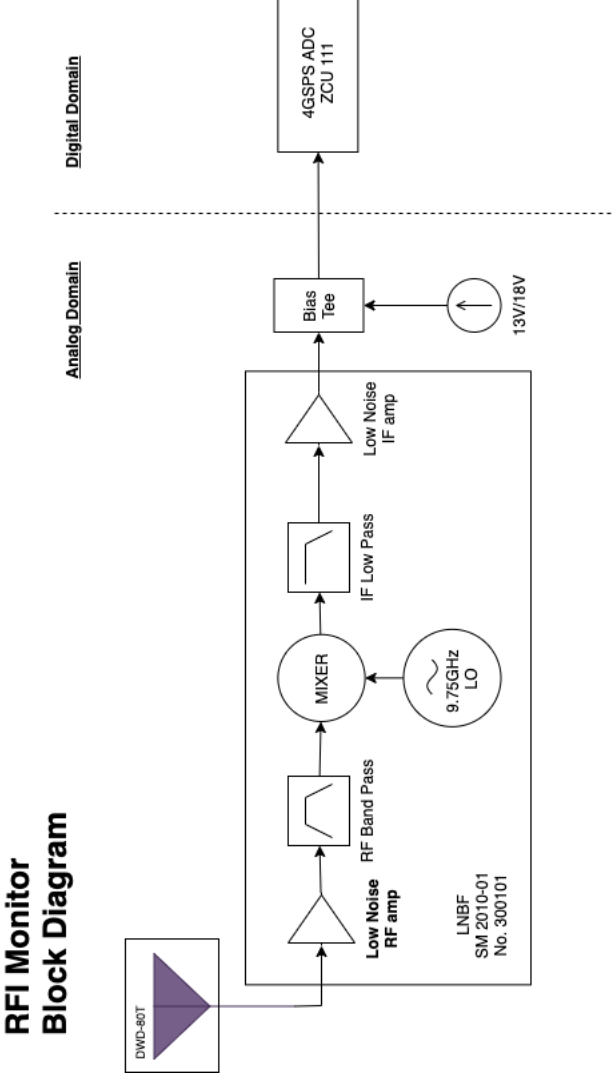


Figure 3.4: A block diagram depicting the high level design of the RFI monitor. The left most component in the diagram corresponds to the television dish the will be used for the system. The dish is an off-axis, 33 inch diameter, parabolic reflector with a housing for an LNB. We used the SatMaximum Universal Single LNB (SM 2010-01) with an integral feed horn and a standard 40mm neck. These LNBs are designed for satellite television receiver dishes and are normally connected to a TV box which mixes down the signal to an intermediate frequency and then decoded. To utilize the LNB in the absence of a TV box we introduce a bias tee between the LNB and the ADC acquisition system. The LNB accepts two settings inputs: a DC current level of 13V or 18V to switch between horizontal and linear polarization setting respectively. The local oscillator frequency is controlled by an input tone of 0KHz or 22KHz corresponding to a local oscillator frequency of 9.75GHz or 10.6GHz respectively. The output of the bias tee is fed to the ADC on the Xilinx ZCU111 evaluation board. The ADC set to sample the signal at 4GSPS in 8 microsecond bursts.

# Chapter 4

## Results

We took two measurements using our digital acquisition system on the afternoon of March 28th, 2022. The measurement was taken in the alley between the Hennings building and Hebb building at the University of British Columbia. The first measurement was taken with the feed pointing up at the sky manually. The second measurement was taken with the feed pointed downwards manually. Note that we did not couple the feed to a dish for this measurement. The LNB was fed a DC current of 13V setting the local oscillator frequency to  $9.5\text{GHz}$ . The input frequency ranges from 10.7-12.7GHz. Therefore the output frequency of the signal fed to the ADC is 0.95-2.95GHz. The ADC was configured to sample at its maximum frequency of 4GHz. Due to the mismatch between sampling frequency and the output of the LNB the time stream data suffers from aliasing of Nyquist zone 4 to zone 1, and zone 3 to zone 2. The ADC was set to sample the LNB output signal in 10 bursts of  $8\mu\text{s}$ . The time stream data from the feed oriented upwards is shown in figure 4.1. The time series data for the downward feed oriented configuration is shown in figure 4.2. The voltage data were binned into 1000 bins prior to plotting.

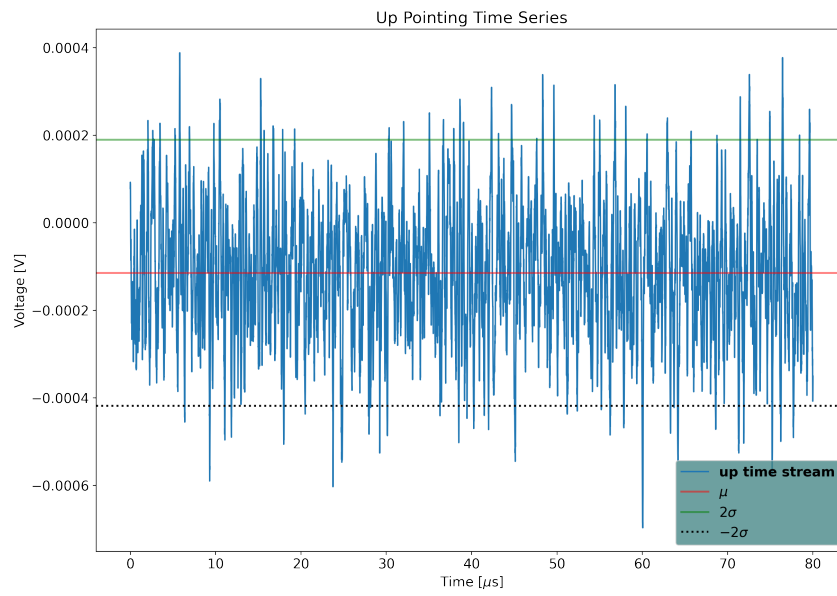


Figure 4.1: The blue curve in the plot corresponds to time series data taken using our digital acquisition system with the feed horn pointed up. We have taken 10 samples each capturing of length  $8\mu\text{s}$ . The blue curve is comprised of 10 of these samples plotted sequentially. The data was binned to 1000 bins prior to plotting. The red horizontal line denotes the average voltage of the up oriented measurement and lies at  $\mu = -0.00011\text{V}$ . The solid horizontal green line corresponds to the voltage two positive deviation from the mean where  $\sigma = 0.00015\text{V}$ . The dashed black line corresponds to the voltage value two negative standard deviations away from the mean. The majority of voltage measurement appear to lie within  $2\sigma$  of the mean value. We do not observe dramatic changes in the voltage that may correspond to strong radio contaminants.

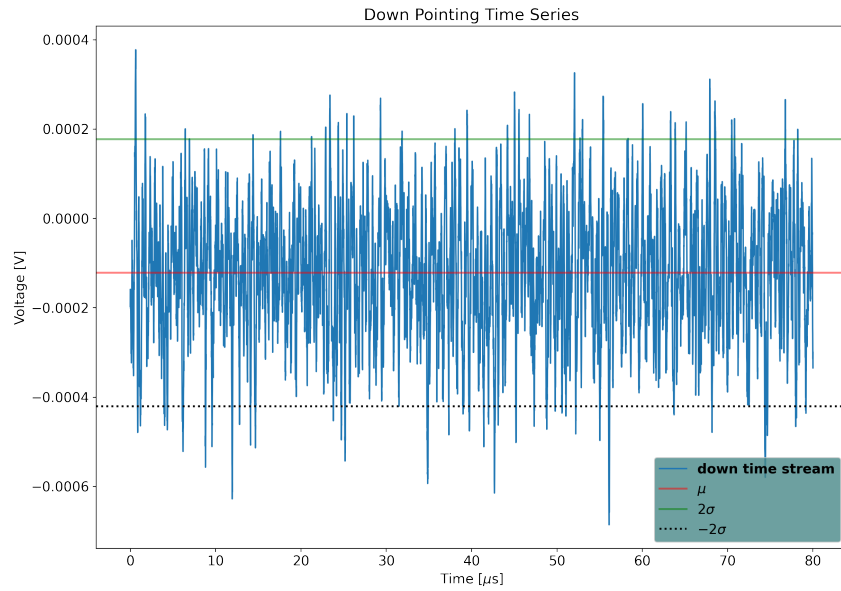


Figure 4.2: The blue curve in the plot corresponds to time series data taken using our digital acquisition system with the feed horn pointed down. The red horizontal line denotes the average voltage of the up oriented measurement and lies at  $\mu = -0.00012\text{V}$ . The solid horizontal green line corresponds to the voltage two positive deviation from the mean where  $\sigma = 0.00015\text{V}$ . The dashed black line corresponds to the voltage value two negative standard deviations away from the mean. The majority of voltage measurement appear to lie within  $2\sigma$  of the mean value. We do not observe dramatic changes in the voltage that may correspond to strong radio contaminants just as in the case of up pointing measurement.

We produced histograms of the time stream data for the up and down measurements. The histograms are binned into 200 bins. A Gaussian fit was preformed for both histograms. A plot of the up pointing histogram with the best fit Gaussian is shown in figure 4.3. The plot the the down pointing measurement time stream data histogram with its best fit Gaussian in shown in figure 4.4.

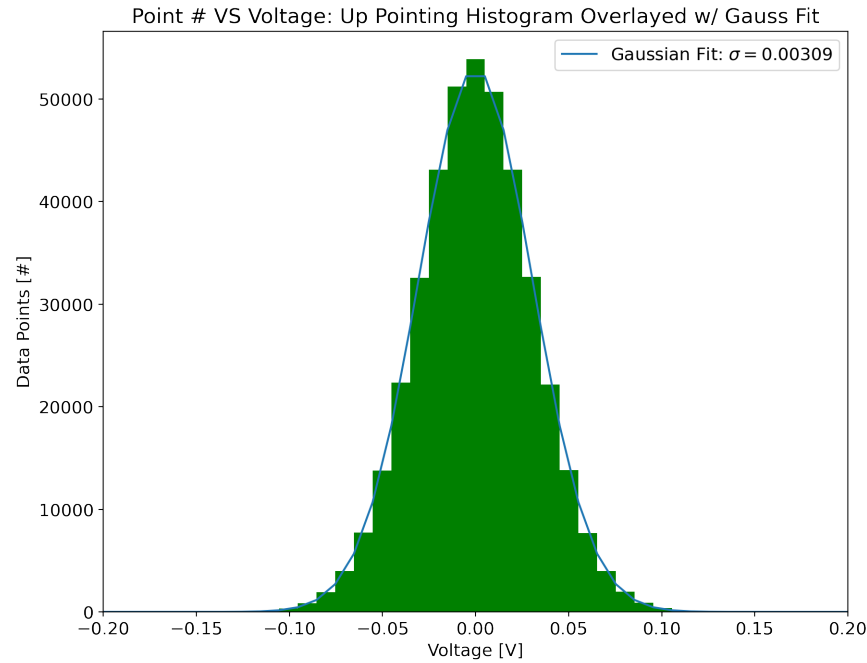


Figure 4.3: Shown in green is a histogram of the voltage time series data binned to 200 bins. The vertical axis measures the counts of occurrences within each voltage bin. The horizontal axis measured the voltage and corresponds to the histogram bins. The curve in blue is a Gaussian fit to the histogram data with  $\sigma = 0.00309$ . The histogram of the up pointing time series data appears to be excellently described by a Gaussian function. We do not observe a high energy tail that could correspond to a radio frequency contaminant in the 10.7-12.7GHz band.

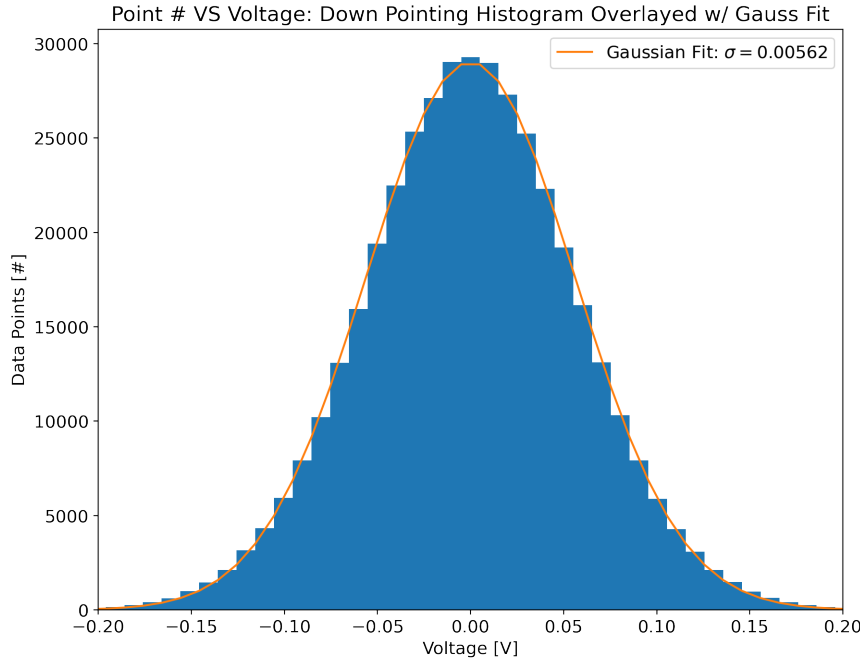


Figure 4.4: Shown in blue is a histogram of the voltage time series data binned to 200 bins. The vertical axis measures the counts of occurrences within each voltage bin. The horizontal axis measured the voltage and corresponds to the histogram bins. The curve in orange is a Gaussian fit to the histogram data with  $\sigma = 0.00562$ . The histogram of the up pointing time series data appears to be excellently described by a Gaussian function. We do not observe a high energy tail that could correspond to a radio frequency contaminant in the 10.7-12.7GHz band just as the histogram of the up pointing measurement time series data.

Power spectra of both time stream data were produced to navigate for the presence of excess power in the form of spikes in the frequency domain. Due to the aforementioned aliasing issue we present plots limited to 0-2GHz. Power contained in Nyquist zones 3-4 corresponding to the 2-4GHz is mirrored into the 0-2GHz making the former frequency window redundant. A combined plot of the real part of the Fourier transform of our time series data as a function of frequency is shown in figure 4.5.

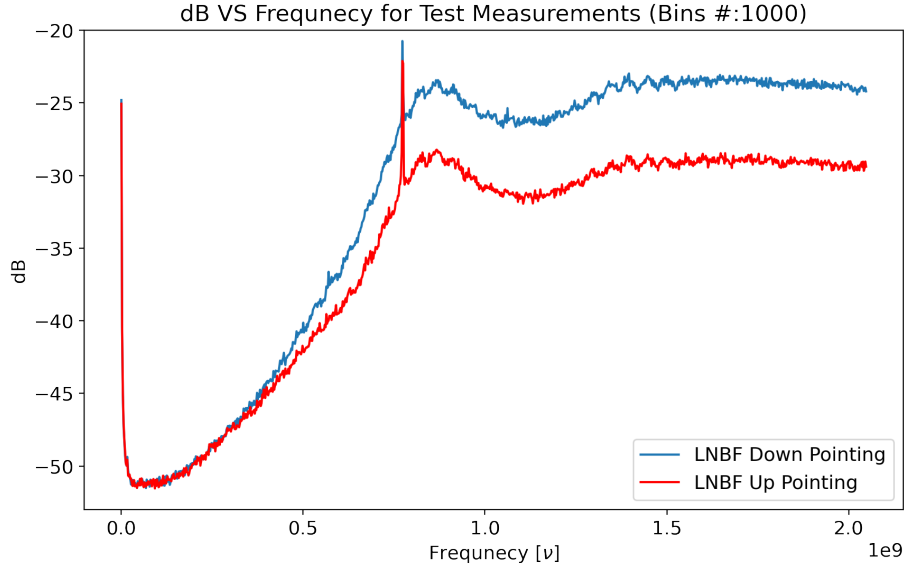


Figure 4.5: The blue curve corresponds to the real part of the Fourier transform of the time series data obtained by pointing the horn feed down. The red curve is the real part of the Fourier transform of the time series data obtained by pointing the horn feed up. The plot truncated the Fourier transform at half the sampling frequency of our ADC system (4GHz). The real Fourier components are provided in units of dB as a function of frequency. We see a rise in power between 0-1GHz. This behavior may be accounted for by the side bands of the LNB. We see that in the range between 1-2GHz the power intercepted from the down pointing measurement exceeds the power intercepted from the up pointing measurement by approximately 4-6 dB for all frequencies in that range. This observation strengthens our confidence in the ability of the digital acquisition system to unambiguously distinguish between sources of brightness temperature of order 300K (the earth) and approximately 25K (the sky).

Of specific interest was the difference in power intercepted from the ground (feed pointed down), and the sky(feed pointed up). We produced plots of the difference between power intercepted with the feed pointed down and pointed up at every frequency bin. The power difference plot in units to decibels vs frequency (hertz) is shown in figure 4.6.

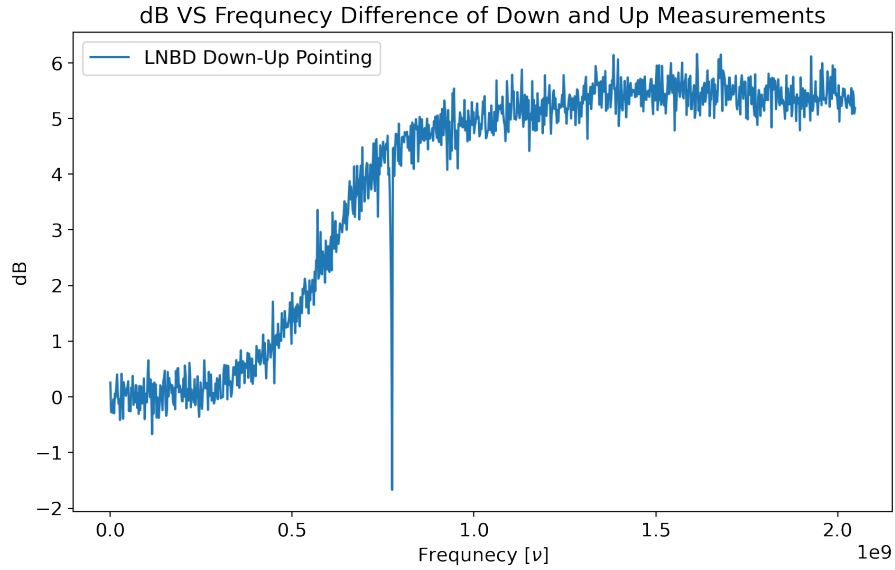


Figure 4.6: The blue curve corresponds to the difference taken between the binned real parts of the FFT of the down and up pointing time series data. The vertical axis measures the power response of our acquisition system in decibels. The horizontal axis measures the frequency in hertz. We observe that the difference between the up and down measurement rises between 0-1GHz until it plateaus at approximately 5 dB for frequencies between 1-2GHz. We interpret this result as an unambiguous difference between the brightness ground and the sky on the order of 5 dB in the frequency range between 10.7-12.7 GHz corresponding to the input frequency of the LNBF.

# Chapter 5

## Discussion

We created an interference monitor simulator that takes orbital parameters of satellites, a scan strategy, and a telescopes parameters and simulates time ordered data. The underlying model uses the SGP4 algorithm to solve for the state vectors of the satellites. Using these state vectors and approximating the satellites as omni directional emitters we derive the expected power intercepted by the telescopes dish at any point in time. To test this model and to conduct a site survey for the upcoming Canadian Galactic Emission Mapper we constructed a digital acquisition system. The digital acquisition system is hosted on the ZCU111 evaluation board. The nominal frequency band of CGEM is 8-10GHz. The 2GHz bandwidth sets a lower limit on the sampling frequency of the ADC at 4GHz. The current digital back-end realization is capable of sampling an incoming signal at 4GHz in bursts of  $8\mu\text{s}$ . We deployed the system at the University of British Columbia for a test run. This preliminary test measurement aimed at unambiguously measuring the power intercepted from two sources which we expect to have different spectra. We chose to point the feed at the sky and at the ground. We report a difference of approximately 5 dB between the down and up measurements for all frequency bins in the range of 1-2GHz. We observe a sloped response of power with respect to frequency on the range of 0-1GHz. A possible interpretation of this behavior can be attributed to the side bands of the band pass filter of the LNB. The output of the LNB is in the range of 0.95-1.95GHz with the current local oscillator setting. The rise in the 0-1GHz could be an observation of the side band increasing towards to nominal range of the band limited signal. To avoid such ambiguities it is necessary to reconfigure the LNB to use only the 0.5-2.5 GHz range. This would also allows us to discern the true frequency of any structure in the power spectra without the concern of aliasing. Nevertheless, the unambiguous measurement of power excess in the measurement of the ground increases our confidence of the digital acquisition system to discern between sources of order of brightness of the sky (approximately 25K) and the ground (approximately 300K). The histograms of the time series data appear to be well described by a Gaussian distribution with a width of 0.0056V for the

## *Chapter 5. Discussion*

---

down measurement and 0.00309V for the up measurement. Taking the ratio of the two and raising it to the power of two to approximate the difference in the spread of power we arrive at 3.28 dB. This is an underestimate compared to the value derived from the difference plot of the binned power spectra. However, the numbers lie within the same order of magnitude. A more appropriate comparison would require a consideration of the bin sizes used for the two types of analysis. The test experiment was designed to measure two sources that we know to have different power responses a priori. We did not attempt to correlate simulated time stream data and the up test time stream data. Prior to attempting a correlation between measured data and the model we must understand the noise floor of the combined digital and analog systems. Future iterations of the experiment will proceed with measurements aimed at understanding the noise level of the system.

# Chapter 6

## Conclusion

We observe a non ambiguous difference of approximately 5 dB between the real part of the Fourier transform of time stream of taken of the ground and the that taken of the sky using our acquisition system. An inspection of the histograms of the up and down pointing time series voltage data appears to be well described by a Gaussian distribution most likely characterizing thermal noise in the system. We do not observe a high energy tail or deviation from the Gaussian functional form that could be characteristic of strong radio contaminants. The digital acquisition system in its current configuration is capable of unambiguously measuring sources with brightness difference on the order of the ground and the sky. Although the understating of true proportion of power coming from the solid angle corresponding to the sky is hindered by our lack of understanding of the beam response of the LNBF. Future iterations of the experiment will need to improve the time coverage of samples taken by the system. The local oscillator of the LNBF needs to be set for the it to output in the 0-2GHz range to avoid aliasing. The immediate next step is to measure the noise floor of the combined digital-analog system. A calibration of the system is also necessary to translate system power to flux units incoming from the source. This would require the measurement of the beam response of the LNBF as well. After then the system can be deployed at the CGEM site for an RFI survey and the time stream could be used to verify the satellite interference model.

# Bibliography

- [1] "Skao Needs Corrective Measures from Satellite 'Mega-Constellation' Operators to Minimise Impact on Its Telescopes." Public Website, 7 Oct. 2020, <https://www.skatelescope.org/news/skao-satellite-impact-analysis/>.
- [2] Info@noirlab.edu. "Starlink Satellites Imaged from CTIO." [Www.noirlab.edu](https://noirlab.edu/public/images/iotw1946a/), <https://noirlab.edu/public/images/iotw1946a/>.
- [3] "WorldVu Satellites Limited, Debtor-in-Possession, Petition for Declaratory Ruling Granting Access to the U.S. Market for the OneWeb Non-Geostationary Satellite Orbit Fixed-Satellite Service V-Band System", Aug 26, 2020, <https://www.fcc.gov/document/fcc-grants-oneweb-us-market-access-expanded-ngso-constellation>
- [4] "FCC Authorizes SpaceX to Provide Broadband Satellite Services", Mar 29, 2018, <https://www.fcc.gov/document/fcc-authorizes-spacex-provide-broadband-satellite-services>
- [5] "FCC Authorizes Kuiper Satellite Constellation", Jul 30, 2020, <https://www.fcc.gov/document/fcc-authorizes-kuiper-satellite-constellation>
- [6] "Application for Fixed Satellite Service by Space Exploration Holdings, LLC", March 29, 2018, <https://fcc.report/IBFS/SAT-LOA-20161115-00118>
- [7] Chapter 3 Radio Telescopes and radiometers. 3 Radio Telescopes and Radiometers Essential Radio Astronomy. (n.d.). Retrieved November 23, 2021, from <https://www.cv.nrao.edu/sransom/web/Ch3.html>.
- [8] "SPACETRACK REPORT NO. 3: Models for Propagation of NORAD Element Sets", December,31 1988, <https://celestrak.com/NORAD/documentation/spacetrk.pdf>

## Bibliography

---

- [9] "Information Regarding Power Flux Density, Revision 2", 2016-07-22, <https://fcc.report/ELS/Space-Exploration-Technologies-Corp/0356-EX-PL-2015>
- [10] Peter Szabó and Katarína Gombíková (2019). Keplerian Orbit, <https://www.mathworks.com/matlabcentral/fileexchange/72098>, MATLAB Central File Exchange., Retrieved November 23, 2021.
- [11] "Chetvorno, CC0, via Wikimedia Commons", <https://commons.wikimedia.org/wiki/File:Dipole-receiving-antennas-animation-6-800x394x150ms.gif>, Retrieved November 23, 2021.
- [12] "The Effects of Earth's Upper Atmosphere on Radio Signals", <https://radiojove.gsfc.nasa.gov/education/activities/iono.html>, Retrieved November 23, 2021.
- [13] "The Kessler Syndrome, As Discussed by Donald J. Kessler", <https://aquareid.physics.uwo.ca/kessler/KesSym.html>, UWO, "Kessler, Donald J"
- [14] "Payload to Launch Ratio", <https://www.space-track.org/spaceOpsTempo>, Public Catalog
- [15] Thiele, S. & Boley, A. Investigating the risks of debris-generating ASAT tests in the presence of megaconstellations. *ArXiv E-prints*. pp. arXiv:2111.12196 (2021,11)
- [16] Swerdlow, N. Kepler's Iterative Solution to Kepler's Equation. *Journal For The History Of Astronomy*. **31**, 339-341 (2000),
- [17] Vallado, D. & Crawford, P. SGP4 Orbit Determination. *AIAA/AAS Astrodynamics Specialist Conference And Exhibit.*, <https://arc.aiaa.org/doi/abs/10.2514/6.2008-6770>
- [18] MacEachern, Josh. CGEM: Notes on Coordinate Systems. *Internal Document*.
- [19] SSC Equivalent Power Flux Density Limits (EPFD) by SSC ITU-R. *ITU World Of Telecommunication Seminar 2018.*, <https://www.itu.int/en/ITU-R/space/WRS18space/WRS18-EPFD-06122018.pdf>
- [20] Xilinx Zynq ultrascale+ rfsoc ZCU111 evaluation kit. *Xilinx.*, <https://www.xilinx.com/products/boards-and-kits/zcu111.html>

## Bibliography

---

- [21] Wiltshire, W. FCC.report. *Application For Fixed Satellite Service By Space Exploration Holdings, LLC.*, <https://fcc.report/IBFS/SAT-MOD-20200417-00037>